Continuum Skyrme Hartree-Fock-Bogoliubov theory with Green's function method for neutron-rich Ca, Ni, Zr, Sn isotopes

En-Bo Huo,[1] Ke-Ran Li,[1] Xiao-Ying Qu,[2] Ying Zhang,[3] and Ting-Ting Sun[1,*]

[1]*School of Physics and Microelectronics, Zhengzhou University, Zhengzhou 450001, China*
[2]*School of Mechatronics Engineering, Guizhou Minzu University, Guiyang 550025, China*
[3]*Department of Physics, School of Science, Tianjin University, Tianjin 300072, China*

(Dated: April 11, 2023)

The possible exotic nuclear properties in the neutron-rich Ca, Ni, Zr, and Sn isotopes are examined with the continuum Skyrme Hartree-Fock-Bogoliubov theory in the framework of Green's function method. The pairing correlation, the couplings with continuum, and the blocking effects for the unpaired nucleon in odd-A nuclei are properly treated. The Skyrme interaction SLy4 is adopted for the *ph* channel and the pairing interaction DDDI is adopted for the *pp* channel, which well reproduce the experimental two-neutron separation energies S_{2n} and one-neutron separation energies S_n. It is found that the criteria $S_n > 0$ predicts a neutron drip line with much smaller neutron numbers than that of $S_{2n} > 0$. Due to the the unpaired odd neutron, neutron pairing energies $-E_{pair}$ in odd-A nuclei are much smaller than the neighboring even-even nuclei. By investigating the single-particle structures, the possible halo structures in the neutron-rich Ca, Ni, and Sn isotopes are predicted, where a sharp increase of rms radii with significant deviations from the traditional $r \propto A^{1/3}$ rule and diffuse spatial distributions in densities are observed. By analyzing the contributions of various partial waves to the total neutron density $\rho_{lj}(r)/\rho(r)$, the orbitals located around the Fermi surface especially those with low angular momenta play significant roles in the extended nuclear density and large rms radii. The number of the neutrons N_λ (N_0) occupying above the Fermi surface λ_n (continuum threshold) are discussed, the evolution of which as a function of the mass number A in each isotopes consist with those of pairing energy, supporting the key role of pairing correlation in halo phenomena.

PACS numbers: 21.60.-n, 21.10.Gv, 21.10.-k, 21.60.Jz

I. INTRODUCTION

The study of exotic nuclei far from the β stability line is a very challenging frontier topic in nuclear physics experimentally [1–4] and theoretically [5–10]. The unstable nuclei with extreme N/Z ratios, which are weakly bound systems, have shown many exotic properties being different from the stable nuclei, such as the halo structures [11–17], the changes of traditional magic numbers [18–23], and new nuclear excitation modes [24, 25], which may also herald new physics. The study of exotic nuclei is not only crucial for the fully understanding of the rich nuclear structures and properties, but also important for the investigations of element synthesis and nuclear astrophysics [26]. However, due to the extreme short lifespan, the cross sections for synthesizing exotic nuclei are extremely small, which makes it extremely difficult to create them experimentally. As a result, more and more advanced large-scale radioactive beam facilities and updated detector techniques have been built, upgraded, or planned in the worldwide [27–34]. Meanwhile, abundant theoretical studies of exotic nuclei provide a useful way for the layout of experiments and analysis of experimental results [35–37].

In the exotic nuclei, especially the drip line nuclei, the neutron or proton Fermi surfaces are usually very close to the continuum threshold. With the effects of the pairing correlation, the valence nucleons have a certain probability to be scattered into the continuum and occupy the resonant states therein, making the nuclear density distributions very diffuse and extended. It is therefore essential to treat the pairing correlations and the couplings to continuum properly in the theoretical descriptions of exotic nuclei [38–42]. Besides, in the one-neutron halo nuclei, such as ^{31}Ne [43] and ^{37}Mg [44], the blocking effect [45] should also be considered to treat the unpaired odd nucleon.

The Hartree-Fock-Bogliubov (HFB) theory has achieved great successes in describing exotic nuclei with a unified description of the mean field and pairing correlation via Bogoliubov transformation [45]. Different models based on HFB theory have been taken to study the exotic nuclei, such as the Gogny-HFB theory [46], the Skyrme-HFB theory [47], the relativistic continuum Hartree-Bogoliubov (RCHB) theory [39], and the density dependent relativistic Hartree-Fock-Bogoliubov (RHFB) theory [48]. To explore the halo phenomena in deformed nuclei, these models have been extended to the deformed framework, such as the deformed relativistic Hartree-Bogoliubov (DRHB) theory [16, 49, 50] and the coordinate-space Skyrme-HFB approach [51–54].

Traditionally, these H(F)B equations are often solved in configuration spaces, i.e., the basis expansion method [55]. However, the calculations are strongly re-

*Electronic address: ttsunphy@zzu.edu.cn

lated to the space size and the shape of the expanded basis. For the harmonic oscillator basis, which has a tail in a shape of Gaussian function, although it is very efficient to describe the stable nuclei, significant difficulties were encountered when applying to exotic nuclei. Bases with proper shapes, such as the Woods-Saxon basis [56] and the transformed harmonic oscillator basis [57, 58] are often taken for the exotic nuclei. For example, to explore deformed halos [59, 60], the DRHB theory based on a Woods-Saxon basis [16, 49] has been developed. In contrast with the basis expansion method, solving the HFB equation in the coordinate space is believed to be more effective. In the coordinate space, discretized method with the box boundary condition has been widely used, by which a series of discrete quasiparticle levels can be obtained easily. However, some flaws have been identified for this method, such as the nonphysical drop of the nuclear densities at the box boundary, the continua and resonant states are discretized, and some unphysical states are included. In contrast, the Green's function (GF) method [61–63] in the coordinate space can avoid these problems and owns great advantages, which can describe the asymptotic behaviors of wave functions properly, provide the energies and widths of the resonant states directly, and treat the bound states and the continua on the same footing.

Due to these advantages, the Green's function method has been applied extensively in nuclear physics to study the contribution of the continuum to the nuclear structures and excitations. As early as in 1987, Belyaev *et al.* have constructed the Green's function for the HFB equation [64]. Afterwards, this HFB Green's function was applied to the quasiparticle random-phase approximation (QRPA) [65], which was further used to describe the collective excitations coupled to the continuum [66–71]. In 2009, the continuum HFB theory in a coupled channel representation was developed to explore the effects of the continuum and pairing correlation in deformed neutron-rich Mg isotopes [72]. In 2011, Zhang *et al.* developed the fully self-consistent continuum Skyrme-HFB theory with Green's function method [73], which was further applied to investigate the giant halos [74] and the effects of pairing correlation on the quasiparticle resonances [75, 76]. In 2019, to explore the halo phenomena in the neutron-rich odd-A nuclei, the self-consistent continuum Skyrme-HFB theory was further extended by including the blocking effect [77]. In recent years, Green's function method has also been adopted for the covariant density functional theory (CDFT) [78–86] in the studies of nuclear structure. For example, by introducing the Green's function method to the relativistic mean filed theory (GF-RMF), the single-particle level structures including the bound states and resonant states and the pseudospin symmetries therein are investigated for neutrons [87, 88], protons [89], and Λ hyperons [90]. Besides, it has been confirmed that exact values of the energies and widths could be obtained by searching for the poles of Green's function or the extremes of the density of states in disregard of the widths of resonant states [91, 92]. By combining the Green's function method with the RCHB theory, the pairing correlation and continuum are well described in the giant halos of the Zr isotopes [93]. By extending the GF-RMF model to the coupled channel representation, the halo candidate nucleus ^{37}Mg reported experimentally is analyzed and confirmed to be a p-wave one-neutron halo according to the Nilsson levels [94]. In addition, the complex-scaled Green's function method [95] has been established as a powerful tool for the exploration of resonant states, which was further extended to the framework of relativistic mean field [96] and the deformed nuclei [97]. Besides, the RMF-CMR-GF approach has been developed by combining the complex momentum representation method with the Green's function method in the relativistic mean-field framework to study the halo structures in the neutron-rich nuclei [98]. All those works have proved the great successes of Green's function method in the descriptions of the continuum.

In this paper, the neutron-rich Ca, Ni, Zr, and Sn isotopes are investigated systematically taking the continuum Skyrme-HFB theory formulated with the Green's function method in the coordinate space, which has treated the pairing correlations, the couplings with continuum, and the blocking effect for the odd unpaired nucleon properly. The paper is organized as follows: In Sec. II, we introduce briefly the continuum Skyrme-HFB theory. Numerical details are presented in Sec. III. After giving the results and discussions in Sec. IV, conclusions are drawn in Sec. V.

II. THEORETICAL FRAMEWORK

In the Hartree-Fock-Bogoliubov (HFB) theory [45], the pair correlated nuclear system is described in terms of independent quasiparticles by the Bogoliubov transformation. The HFB equation in the coordinate space [38] is,

$$\begin{pmatrix} h-\lambda & \tilde{h} \\ \tilde{h}^* & -h^*+\lambda \end{pmatrix} \phi_i(\boldsymbol{r}\sigma) = E_i\phi_i(\boldsymbol{r}\sigma), \qquad (1)$$

where E_i is the quasiparticle energy, $\phi_i(\boldsymbol{r}\sigma)$ is the quasiparticle wave function, and λ is the Fermi energy determined by constraining the expectation value of the nucleon number. The HF Hamiltonian $h(\boldsymbol{r}\sigma,\boldsymbol{r}'\sigma')$ and the pair Hamiltonian $\tilde{h}(\boldsymbol{r}\sigma,\boldsymbol{r}'\sigma')$ are obtained by the variation of the total energy functional with respect to the particle density $\rho(\boldsymbol{r}\sigma,\boldsymbol{r}'\sigma')$ and the pair density $\tilde{\rho}(\boldsymbol{r}\sigma,\boldsymbol{r}'\sigma')$, respectively. The solutions of the HFB equations have two symmetric branches, one is positive ($E_i > 0$) with the quasiparticle wave function $\phi_i(\boldsymbol{r}\sigma)$ while the other is negative ($-E_i < 0$) with the conjugate wave function $\bar{\phi}_{\bar{i}}(\boldsymbol{r}\sigma)$. The wave functions $\phi_i(\boldsymbol{r}\sigma)$ and $\bar{\phi}_{\bar{i}}(\boldsymbol{r}\sigma)$ are in two

components and they are related as,

$$\phi_i(\boldsymbol{r}\sigma) = \begin{pmatrix} \varphi_{1,i}(\boldsymbol{r}\sigma) \\ \varphi_{2,i}(\boldsymbol{r}\sigma) \end{pmatrix}, \quad \bar{\phi}_{\bar{i}}(\boldsymbol{r}\sigma) = \begin{pmatrix} -\varphi^*_{2,i}(\boldsymbol{r}\tilde{\sigma}) \\ \varphi^*_{1,i}(\boldsymbol{r}\tilde{\sigma}) \end{pmatrix}, \quad (2)$$

with $\varphi(\boldsymbol{r}\tilde{\sigma}) = -2\sigma\varphi(\boldsymbol{r}, -\sigma)$. Here and hereafter, we follow the notations in Ref. [65] for convenience.

For an even-even nucleus, the ground state $|\Phi_0\rangle$ is a quasiparticle vacuum with the particle density $\rho(\boldsymbol{r}\sigma, \boldsymbol{r}'\sigma')$ and pairing density $\tilde{\rho}(\boldsymbol{r}\sigma, \boldsymbol{r}'\sigma')$ determined by

$$\rho(\boldsymbol{r}\sigma, \boldsymbol{r}'\sigma') \equiv \langle\Phi_0|c^\dagger_{\boldsymbol{r}'\sigma'}c_{\boldsymbol{r}\sigma}|\Phi_0\rangle, \quad (3a)$$
$$\tilde{\rho}(\boldsymbol{r}\sigma, \boldsymbol{r}'\sigma') \equiv \langle\Phi_0|c_{\boldsymbol{r}'\tilde{\sigma}'}c_{\boldsymbol{r}\sigma}|\Phi_0\rangle, \quad (3b)$$

where $c^\dagger_{\boldsymbol{r}\sigma}$ and $c_{\boldsymbol{r}\sigma}$ are the particle creation and annihilation operators, respectively. The densities can be unified as a generalized density matrix $R(\boldsymbol{r}\sigma, \boldsymbol{r}'\sigma')$, with $\rho(\boldsymbol{r}\sigma, \boldsymbol{r}'\sigma')$ and $\tilde{\rho}(\boldsymbol{r}\sigma, \boldsymbol{r}'\sigma')$ being the "11" and "22" element, respectively. With the quasiparticle wave functions, $R(\boldsymbol{r}\sigma, \boldsymbol{r}'\sigma')$ can be written in a simple form,

$$R(\boldsymbol{r}\sigma, \boldsymbol{r}'\sigma') = \sum_i \bar{\phi}_{\bar{i}}(\boldsymbol{r}\sigma)\bar{\phi}^\dagger_{\bar{i}}(\boldsymbol{r}'\sigma'). \quad (4)$$

For an odd-A nucleus, the last odd nucleon is unpaired, for which the blocking effect should be considered. The nuclear ground state in this case is a one-quasiparticle state $|\Phi_1\rangle$, which can be constructed based on a HFB vacuum $|\Phi_0\rangle$ as

$$|\Phi_1\rangle = \beta^\dagger_{i_\mathrm{b}}|\Phi_0\rangle, \quad (5)$$

where $\beta^\dagger_{i_\mathrm{b}}$ is the quasiparticle creation operator and i_b denotes the blocked quasiparticle level occupied by the odd nucleon. Accordingly, the particle density $\rho(\boldsymbol{r}\sigma, \boldsymbol{r}'\sigma')$ and the pairing density $\tilde{\rho}(\boldsymbol{r}\sigma, \boldsymbol{r}'\sigma')$ are

$$\rho(\boldsymbol{r}\sigma, \boldsymbol{r}'\sigma') \equiv \langle\Phi_1|c^\dagger_{\boldsymbol{r}'\sigma'}c_{\boldsymbol{r}\sigma}|\Phi_1\rangle, \quad (6a)$$
$$\tilde{\rho}(\boldsymbol{r}\sigma, \boldsymbol{r}'\sigma') \equiv \langle\Phi_1|c_{\boldsymbol{r}'\tilde{\sigma}'}c_{\boldsymbol{r}\sigma}|\Phi_1\rangle, \quad (6b)$$

and the generalized density matrix $R(\boldsymbol{r}\sigma, \boldsymbol{r}'\sigma')$ becomes

$$\begin{aligned} R(\boldsymbol{r}\sigma, \boldsymbol{r}'\sigma') &= \sum_{i:\mathrm{all}} \bar{\phi}_{\bar{i}}(\boldsymbol{r}\sigma)\bar{\phi}^\dagger_{\bar{i}}(\boldsymbol{r}'\sigma') \quad (7) \\ &\quad -\bar{\phi}_{\bar{i}_\mathrm{b}}(\boldsymbol{r}\sigma)\bar{\phi}^\dagger_{\bar{i}_\mathrm{b}}(\boldsymbol{r}'\sigma') + \phi_{i_\mathrm{b}}(\boldsymbol{r}\sigma)\phi^\dagger_{i_\mathrm{b}}(\boldsymbol{r}'\sigma'), \end{aligned}$$

where two more terms are introduced compared with those for the even-even nuclei.

In the conventional Skyrme-HFB theory, the HFB equation (1) in the coordinate space is often solved with the box boundary condition, and a series of the discretized eigensolutions including the quasiparticle energy E_i and the corresponding wave functions $\phi_i(\boldsymbol{r}\sigma)$ could be obtained. Then the generalized density matrix $R(\boldsymbol{r}\sigma, \boldsymbol{r}'\sigma')$ can be calculated by summing those discretized quasiparticle states as shown in Eqs. (4) and (7). We call this method the box-discretized approach. However, the applicability of the box boundary condition in the description of exotic nuclei especially those close to the drip line is not good. A large enough coordinate space (or box size) should be taken to describe the very extended density distribution.

Green's function method can avoid these problems of box-discretized approach, which impose the correct asymptotic behaviors on the wave functions, especially for the weakly-bound sates and the continuum. The Green's function $G(\boldsymbol{r}\sigma, \boldsymbol{r}'\sigma'; E)$ with an arbitrary quasiparticle energy E defined for the coordinate-space HFB equation obeys,

$$\begin{aligned} &\left[E - \begin{pmatrix} h-\lambda & \tilde{h} \\ \tilde{h}^* & -h^*+\lambda \end{pmatrix}\right] G(\boldsymbol{r}\sigma, \boldsymbol{r}'\sigma'; E) \\ &\quad = \delta(\boldsymbol{r}-\boldsymbol{r}')\delta_{\sigma\sigma'}, \end{aligned} \quad (8)$$

which is a 2×2 matrix. The generalized density matrix $R(\boldsymbol{r}\sigma, \boldsymbol{r}'\sigma')$ in Eq. (7) can be calculated by the integrals of the Green's function performed on the complex quasiparticle energy plane as

$$\begin{aligned} R(\boldsymbol{r}\sigma, \boldsymbol{r}'\sigma') &= \frac{1}{2\pi i}\left[\oint_{C_{E<0}} dE G(\boldsymbol{r}\sigma, \boldsymbol{r}'\sigma'; E)\right. \\ &\quad - \oint_{C^-_\mathrm{b}} dE G(\boldsymbol{r}\sigma, \boldsymbol{r}'\sigma'; E) \\ &\quad \left. + \oint_{C^+_\mathrm{b}} dE G(\boldsymbol{r}\sigma, \boldsymbol{r}'\sigma'; E)\right], \end{aligned} \quad (9)$$

where the contour path $C_{E<0}$ encloses all the negative quasiparticle energies $-E_i < 0$, C^-_b encloses only the pole of $-E_{i_\mathrm{b}}$, and C^+_b encloses only the pole of E_{i_b}.

In the spherical case, the quasiparticle wave functions $\phi_i(\boldsymbol{r}\sigma)$ and $\bar{\phi}_{\bar{i}}(\boldsymbol{r}\sigma)$ are only dependent on the radial parts, and they can be expanded as

$$\phi_i(\boldsymbol{r}\sigma) = \frac{1}{r}\phi_{nlj}(r)Y^l_{jm}(\hat{\boldsymbol{r}}\sigma), \quad (10a)$$
$$\bar{\phi}_{\bar{i}}(\boldsymbol{r}\sigma) = \frac{1}{r}\bar{\phi}_{nlj}(r)Y^{l*}_{jm}(\hat{\boldsymbol{r}}\tilde{\sigma}), \quad (10b)$$
$$\phi_{nlj}(r) = \begin{pmatrix} \varphi_{1,nlj}(r) \\ \varphi_{2,nlj}(r) \end{pmatrix}, \quad (10c)$$
$$\bar{\phi}_{nlj}(r) = \begin{pmatrix} -\varphi^*_{2,nlj}(r) \\ \varphi^*_{1,nlj}(r) \end{pmatrix}, \quad (10d)$$

where $Y^l_{jm}(\hat{\boldsymbol{r}}\sigma)$ is the spin spherical harmonic, and $Y^l_{jm}(\hat{\boldsymbol{r}}\tilde{\sigma}) = -2\sigma Y^l_{jm}(\hat{\boldsymbol{r}} - \sigma)$. Similarly, the generalized density matrix $R(\boldsymbol{r}\sigma, \boldsymbol{r}'\sigma')$ and the Green's function $G(\boldsymbol{r}\sigma, \boldsymbol{r}'\sigma'; E)$ can be expanded as

$$R(\boldsymbol{r}\sigma, \boldsymbol{r}'\sigma') = \sum_{ljm} Y^l_{jm}(\hat{\boldsymbol{r}}\sigma)R_{lj}(r, r')Y^{l*}_{jm}(\hat{\boldsymbol{r}}'\sigma'), \quad (11a)$$

$$G(\boldsymbol{r}\sigma, \boldsymbol{r}'\sigma'; E) = \sum_{ljm} Y^l_{jm}(\hat{\boldsymbol{r}}\sigma)\frac{\mathcal{G}_{lj}(r, r'; E)}{rr'}Y^{l*}_{jm}(\hat{\boldsymbol{r}}'\sigma'), \quad (11b)$$

where $R_{lj}(r, r')$ and $\mathcal{G}_{lj}(r, r'; E)$ are the radial parts of

the generalized density matrix and Green's function, respectively.

As a result, the radial local generalized density matrix $R(r) = R(r,r)$ can be expressed by the radial HFB Green's function $\mathcal{G}_{lj}(r,r';E)$ as

$$\begin{aligned} R(r) &= \sum_{lj} R_{lj}(r,r) \\ &= \frac{1}{4\pi r^2}\left[\sum_{lj:\text{all}}(2j+1)\sum_{n:\text{all}}\bar{\phi}^2_{nlj}(r) - \bar{\phi}^2_{n_\text{b}l_\text{b}j_\text{b}}(r) \right. \\ &\quad \left. +\phi^2_{n_\text{b}l_\text{b}j_\text{b}}(r)\right] \qquad (12) \\ &= \frac{1}{4\pi r^2}\frac{1}{2\pi i}\left[\sum_{lj:\text{all}}(2j+1)\oint_{C_{E<0}} dE\mathcal{G}_{lj}(r,r;E)\right. \\ &\quad \left. -\oint_{C^-_\text{b}} dE\mathcal{G}_{l_\text{b}j_\text{b}}(r,r;E) + \oint_{C^+_\text{b}} dE\mathcal{G}_{l_\text{b}j_\text{b}}(r,r;E)\right]. \end{aligned}$$

From the radial generalized matrix $R(r)$, one can easily obtain the radial local particle density $\rho(r)$ and pair density $\tilde{\rho}(r)$, which are the "11" and "12" components of $R(r)$, respectively. In the same way, one can express other radial local densities needed in the functional of the Skyrme interaction, such as the kinetic-energy density $\tau(r)$, the spin-orbit density $J(r)$, etc., in terms of the radial Green's function. For the construction of the Green's function, see Refs. [73, 77].

III. NUMERICAL DETAILS

For the Skyrme interaction in the *ph* channel, the SLy4 parameter set [100] is adopted. For the pairing interaction in the *pp* channel, a density dependent δ interaction (DDDI) is taken,

$$v_\text{pair}(\boldsymbol{r},\boldsymbol{r}') = \frac{1}{2}(1-P_\sigma)V_0\left[1-\eta\left(\frac{\rho(\boldsymbol{r})}{\rho_0}\right)^\alpha\right]\delta(\boldsymbol{r}-\boldsymbol{r}'). \qquad (13)$$

The pair Hamiltonian $\tilde{h}(\boldsymbol{r}\sigma,\boldsymbol{r}'\sigma')$ is then reduced to a local pair potential [47],

$$\Delta(\boldsymbol{r}) = \frac{1}{2}V_0\left[1-\eta\left(\frac{\rho(\boldsymbol{r})}{\rho_0}\right)^\alpha\right]\tilde{\rho}(\boldsymbol{r}). \qquad (14)$$

The strength of the pairing force $V_0 = -458.4$ MeV·fm^3, the density $\rho_0 = 0.08$ fm^{-3}, and other parameters $\eta = 0.71$, $\alpha = 0.59$, which are constrained by reproducing the experimental neutron pairing gaps for the Sn isotopes [68, 101, 102]. With these parameters, DDDI can reproduce the scattering length $a = -18.5$ fm in the ^1S channel of the bare nuclear force in the low density limit [101]. The cut-off of the quasiparticle states are taken with maximal angular momentum $j_\text{max} = 25/2$ and the maximal quasiparticle energy $E_\text{cut} = 60$ MeV.

The HFB equation is solved in the coordinate space with the space size $R_\text{box} = 20$ fm and mesh size $dr = 0.1$ fm. To calculate the densities with the Green's function, the integrals of the Green's functions are performed along a contour path $C_{E<0}$, which is chosen as a rectangle with the height $\gamma = 0.1$ MeV and the length $E_\text{cut} = 60$ MeV to enclose all the quasiparticle states with negative energies. For the odd-A nuclei, two more contour paths C^+_b and C^-_b, which only enclose the blocked quasiparticle states at energies E_{i_b} and $-E_{i_\text{b}}$, are introduced due to the blocking effect of the odd unpaired nucleon. For these details, one can refer to Ref. [77]. To do the contour integration, an energy step of $\Delta E = 0.01$ MeV on the contour path is adopted.

IV. RESULTS AND DISCUSSION

In Fig. 1, the two-neutron separation energies $S_{2\text{n}}(N,Z) = E(N-2,Z) - E(N,Z)$ are plotted for the even-even and odd-even Ca, Ni, Zr, and Sn isotopes. Red circles are those calculated by the continuum Skyrme-HFB theory with the SLy4 parameter set, in comparison with the results by the discretized method denoted by the blue triangles and the available experimental data [99] denoted by the black squares. The differences between S_{2n} by the Green's function method and discretized method are found slight. Good agreements with the experimental data could be observed, indicating the reliability of the continuum Skyrme-HFB theory in the prediction of neutron drip line. The traditional shell closures, i.e., $N = 28$ in Ca isotopes, $N = 50$ in Ni isotopes, $N = 50, 82$ in Zr isotopes, and $N = 82$ in Sn isotopes, could also be identified, where the $S_{2\text{n}}$ drops sharply. For example, in the Sn chain, $S_{2\text{n}}$ drops from 13.25 MeV at ^{132}Sn to 4.94 MeV at ^{134}Sn with the neutron number exceeding the magic number $N = 82$. In the Ca, Ni, and Zr chains, the two-neutron separation energies quickly reach zero at large mass range, resulting in relative short neutron drip lines, which are ^{67}Ca, ^{89}Ni, and ^{123}Zr, respectively. On the contrary, in the Sn chain, $S_{2\text{n}}$ keeps less than 1.0 MeV in a wide mass region after the gap of $N = 82$ and finally becomes negative until $A = 178$, suggesting ^{177}Sn is a neutron drip line nucleus. Those weakly bound nuclei are quite interesting due to possible appearance of neutron halos although it is experimentally difficult to reach. In addition, the exploration of the neutron drip line and the determination on the limit of nuclear landscape are significantly important in nuclear physics. However, various theoretical studies show that the predicated neutron drip line is very model dependent [103]. Moreover, different physical quantities or criteria will also predict very different neutron drip lines.

To explore the neutron drip lines in the Ca, Ni, Zr, and Sn isotopes, in Fig. 2 the single-neutron separation energies $S_\text{n}(N,Z) = E(N-1,Z) - E(N,Z)$ are plotted. Results by the continuum Skyrme-HFB theory with the SLy4 parameter set are denoted by red circles, which are consistent well with the experimental data [99] de-

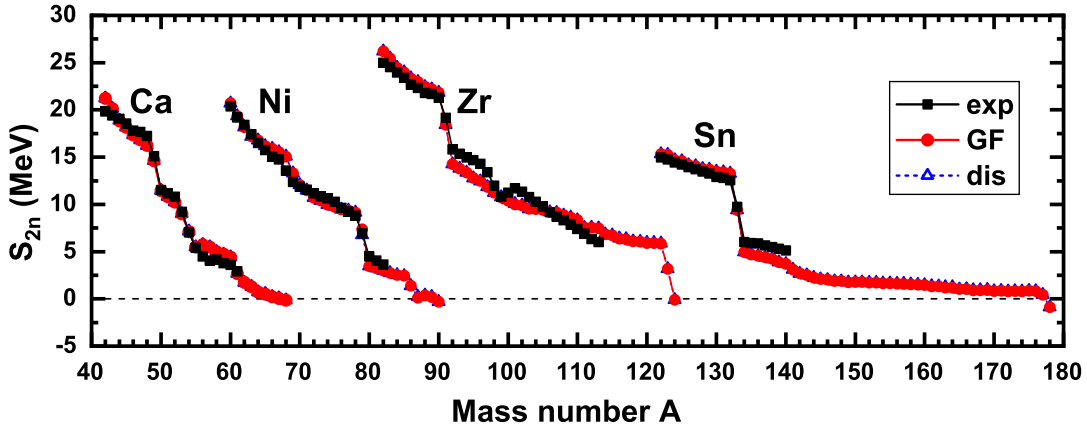

FIG. 1: (Color online) Two-neutron separation energies S_{2n} in the Ca, Ni, Zr, and Sn isotopes as a function of the mass number A calculated by the continuum Skyrme HFB theory with the SLy4 parameter set (filled red circles), in comparison with the results by the discretized method (open blue triangles) and the experimental data (filled black squares) [99].

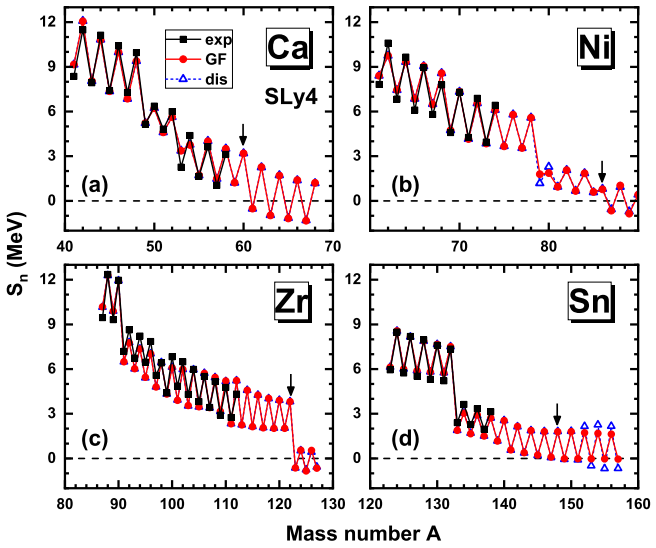

FIG. 2: (Color online) Single-neutron separation energies S_n as a function of the mass number A in the (a) Ca, (b) Ni, (c) Zr, and (d) Sn isotopes calculated by the continuum Skyrme-HFB theory with the SLy4 parameter set (filled red circles), in comparison with the results by the discretized method (open blue triangles) and the experimental data (filled black squares) [99].

noted by the black squares. Strong odd-even staggering is observed in all isotopes. In general, the S_n in the even-even nucleus is around $2 \sim 3$ MeV larger than the neighbouring odd-A nuclei, which is attributed to the unpaired odd neutron with vanishing pairing energy. As a result, compared with those in Fig. 1, the neutron drip lines determined by the one-neutron separation energy are greatly shortened. In the Ca, Ni, Zr, and Sn isotopes, the drip line nuclei are ^{60}Ca, ^{86}Ni, ^{122}Zr, and ^{148}Sn, respectively, the positions of which are indicated by the black arrows. Outside the neutron drip line determined by S_n, the bound even-even nuclei behave as the interesting Borromean systems. For example, based on the bound nucleus ^{60}Ca, ^{60}Ca+n is unbound while ^{60}Ca+$n+n$ is bound.

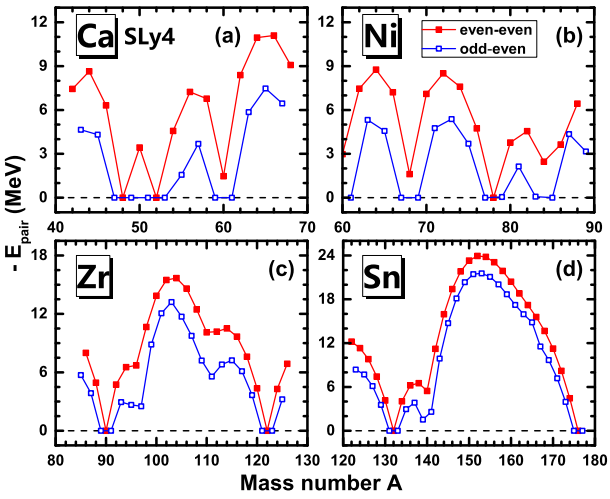

FIG. 3: (Color online) Neutron pairing energy $-E_{\rm pair}$ as a function of the mass number A in the (a) Ca, (b) Ni, (c) Zr, and (d) Sn isotopes calculated by the continuum Skyrme-HFB theory with the SLy4 parameter set. The filled and open squares represent the results of the even-even and odd-even nuclei, respectively.

In Fig. 3, we plot the neutron pairing energy $E_{\rm pair}$, which is expressed as,

$$E_{\rm pair} = \frac{1}{2}\int d\boldsymbol{r}\Delta(\boldsymbol{r})\tilde{\rho}(\boldsymbol{r}). \quad (15)$$

The red solid symbols are for the even-even nuclei and open symbols for the odd-A nuclei. The neutron pairing energies $E_{\rm pair}$ for the odd-A nuclei are much smaller than those of the neighboring even-even nuclei, due to the ab-

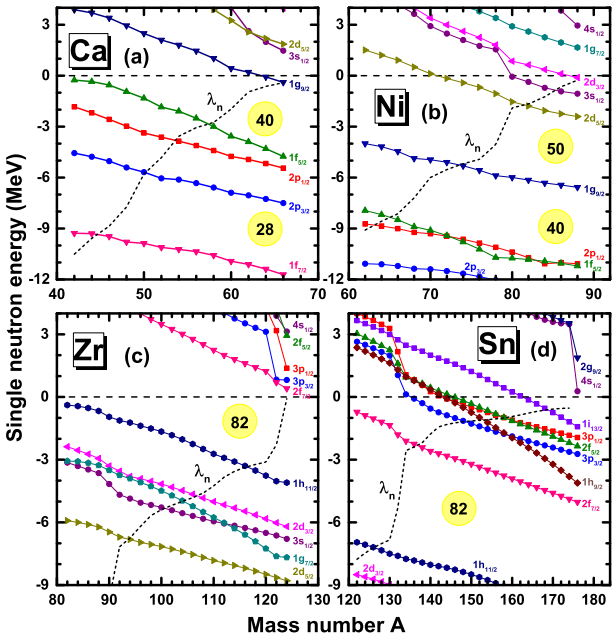

FIG. 4: (Color online) Single-particle levels for neutrons around the Fermi surface in the canonical basis for the (a) Ca, (b) Ni, (c) Zr, and (d) Sn isotopes calculated by the continuum Skyrme-HFB theory. The short dashed lines represent the Fermi surface.

sent contribution of pairing energy by the unpaired neutron. This also explains why the drip line determined by the single-neutron separation energy $S_{\rm n}$ is much shorter than that obtained by the two-neutron separation energy $S_{2\rm n}$. In addition, obvious shell effects are shown in the pairing energy. For example, in the Sn isotopes, zero pairing energies at $N = 82$ and $N = 126$ while reaching the largest value at half shell $N = 102$ could be observed. As a result, the traditional shell closures, i.e., $N = 28, 40$ in Ca isotopes, $N = 40, 50$ in Ni isotopes, $N = 50, 82$ in Zr isotopes, and $N = 82, 126$ in Sn isotopes, could also be obviously observed, which are consistent with those obtained in Fig. 1. In addition, a sub-shell $N = 32$ is also observed in Ca isotopes.

In the following, the possible neutron halos in the Ca, Ni, Zr, and Sn isotopes are examined, especially in the weakly bound nuclei close to the neutron drip line, in which the Fermi surfaces are very close to the continuum threshold and the valence neutrons could be easily scattered to the continuum.

In Fig. 4, the neutron canonical single-particle structure as functions of the mass number are plotted for the (a) Ca, (b) Ni, (c) Zr, and (d) Sn isotopes. For more details on obtaining the canonical single-particle levels, please refer to Refs. [104, 105]. The neutron Fermi energy $\lambda_{\rm n}$ as well as the canonical single-particle energies ε are shown. As the neutron number increasing, the Fermi energy $\lambda_{\rm n}$ in each chain is raised up and finally reaches the continuum threshold while all the HF single-particle levels decreases. The traditional shell closures, i.e., $N = 28, 40$ in Ca isotopes, $N = 40, 50$ in Ni isotopes, $N = 82$ in Zr isotopes, and $N = 82$ in Sn isotopes, could be observed, where the big gaps could be observed obviously. Different single-particle structures are revealed in Ca, Ni, Zr, and Sn chains, based on which halos may be formed. In the Ni chain, above the shell closure of $N = 50$, there are several weakly bound states and low-lying positive canonical states in the continuum with small angular momenta, which favor the formation of halos. For example, in ^{86}Ni, around the Fermi surface, there are two weakly bound states, $2d_{5/2}$ and $3s_{1/2}$, and one low-lying positive canonical state $2d_{3/2}$. The Sn chain is quite similar to the Ni chain but has more advantages for halo formation, where weakly bound states and the low-lying positive states in the continuum exist above the $N = 82$ shell closure. Besides, the Fermi surface $\lambda_{\rm n}$ approaches to zero gradually and the Sn isotopes in a large mass region are weakly bound. In the Ca chain, above the shell closure of $N = 40$, there is mainly the $1g_{9/2}$ state, which evolves from a canonical positive state in the continuum ($A \leq 62$) to a weakly bound level ($A \geq 64$). Although there is a possibility for valence neutrons occupying $1g_{9/2}$ orbital, the contributed density is very localized due to the big central barrier. In the neutron-rich Ca isotopes, the low-lying positive canonical states in the continuum $3s_{1/2}$ and $2d_{5/2}$ also play important roles. The formation of halos is most unlikely for Zr chain where the shell closure of $N = 82$ is located around the threshold of continuum and it's hard for the valence neutrons to overcome the large gap and occupy the continuum.

In Fig. 5, the neutron root-mean-square (rms) radii

$$r_{\rm rms} = \sqrt{\frac{\int dr 4\pi r^4 \rho(r)}{\int dr 4\pi r^2 \rho(r)}}, \tag{16}$$

are plotted for the Ca, Ni, Zr, and Sn isotopes, which are obtained by the Skyrme-HFB calculations both with the Green's function method (filled circles and solid lines) and box-discretized method (open triangles and dashed lines) employing the SLy4 parameter set. The radii $r = b_0 A^{1/3}$ in the traditional liquid-drop model (black lines) are indicated as well, where the coefficient b_0 could be determined by the radii of deeply bound nuclei. In the Ca, Ni, Zr, and Sn chains, they are $r \approx 0.991A^{1/3}$, $0.984A^{1/3}$, $0.957A^{1/3}$, and $0.961A^{1/3}$, respectively. In each chain, by adding more neutrons, the nuclear rms radii $r_{\rm rms}$ increase steeply and deviate from the radii $A^{1/3}$ rule. For example, in the Ca chain, compared with the isotopic trend in $N \leqslant 20$ with $r \approx 0.991A^{1/3}$, the neutron rms radii in ^{50}Ca and the heavier isotopes display steep increases with N. In those mass area, possible neutron halos may occur. Besides, obvious odd-even staggering of rms radii could be observed in the Sn chain, where the odd-A nuclei $^{151-165}$Sn own larger rms radii than the neighbouring two even-even nuclei. The detailed explanations could be found in Ref. [77]. The odd-even staggering phenomena in nuclear radii and nu-

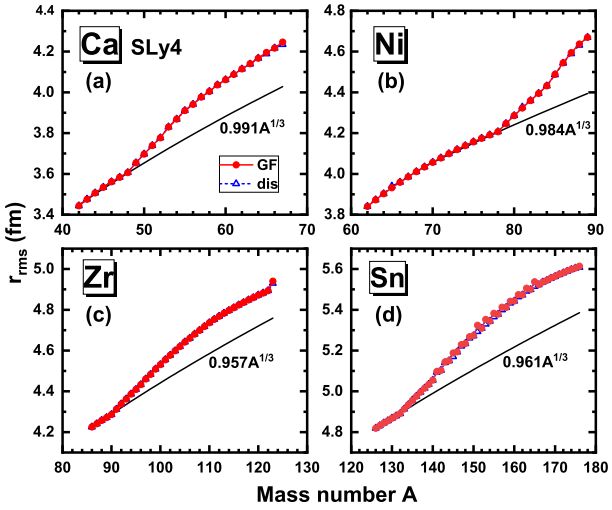

FIG. 5: (Color online) Neutron root-mean-square (rms) radii $r_{\rm rms}$ for the (a) Ca, (b) Ni, (c) Zr, and (d) Sn isotopes calculated by the Skyrme-HFB theory with the Green's function method (filled circles and solid lines), in comparison with the results by the discretized method (open triangles and dashed lines).

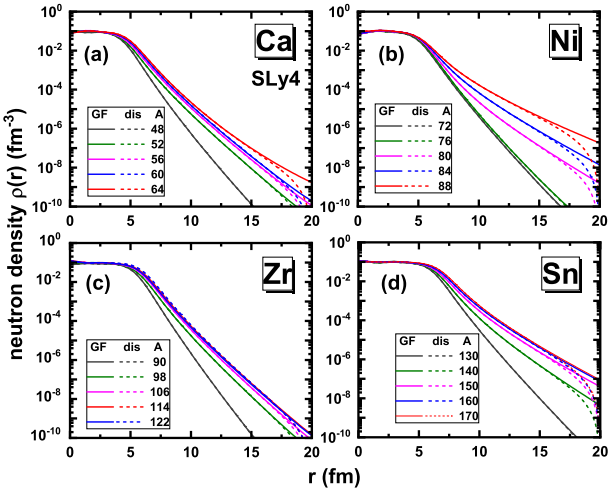

FIG. 6: (Color online) Neutron density $\rho(r)$ for the (a) Ca, (b) Ni, (c) Zr, and (d) Sn isotopes calculated by the Skyrme-HFB theory with the Green's function method (solid lines), in comparison with the results by the discretized method (dashed lines).

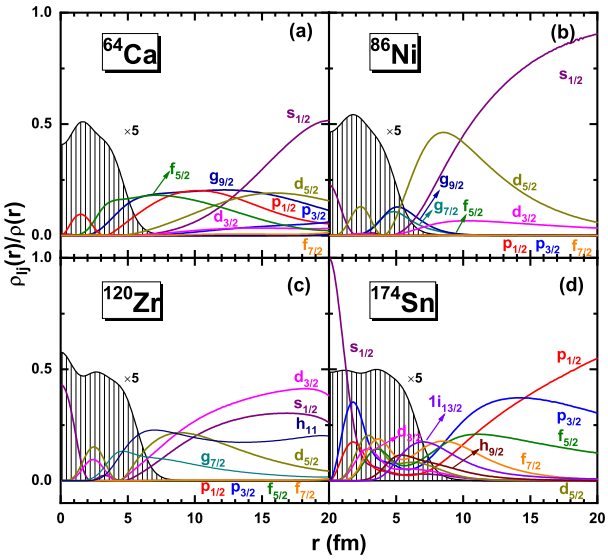

FIG. 7: (Color online) Contributions of different partial waves to the total neutron density, $\rho_{lj}(r)/\rho(r)$, as a function of the radial coordinate r for the neutron-rich nuclei (a) ^{64}Ca, (b) ^{86}Ni, (c) ^{120}Zr, and (d) ^{174}Sn. The shallow regions are for the nuclear density distributions $\rho(r)$, which are rescaled by multiplying a factor of 5.

clear mass have attracted great interests in the past years and lots of efforts have been done, such as the works in Refs. [106–112].

In the exotic nuclei, diffuse density distributions in the coordinate space is often observed. Thus, in Fig. 6, to explore the exotic structures in the (a) Ca, (b) Ni, (c) Zr, and (d) Sn isotopes, we also plot the neutron density distributions $\rho(r)$, where the solid lines are those obtained by the Green's function method in comparison with the results by the box-discretized method denoted by the dashed lines. It is a global trend that the neutron density distributions are extended further with the increasing neutron number. The shell structures influence the density distribution significantly, i.e., compared with the bound nuclei, the density distributions of the neutron-rich nuclei in the (a) Ca, (b) Ni, (c) Zr, and (d) Sn isotopes with the neutron number exceeding the neutron closure $N = 28, 50, 50, 82$ are much more extended, which is consistent with the behaviors of the rms radii plotted in Fig. 5. In addition, compared with the Ca and Zr chains, the Ni and Sn chains exhibit more diffuse distributions in densities, which can be explained by their small two-neutron separation energies S_{2n} in a large mass range plotted in Fig. 1. In the case of the Zr isotopes, the density distributions are relatively localized. In combination with the large S_{2n} plotted in Fig. 1, we are inclined to believe the absence of halos in Zr isotopes. However, taking the RCHB theory with the NLSH parameter set [113] and the continuum Skyrme-HFB theory with the SKI4 parameter set [74, 114], giant halos in Zr isotopes have been predicated. In all isotopes, compared with the box-discretized method predicting nonphysical sharp decreases of densities at the space boundary, Green's function method can describe well the extended density distributions, especially for the very neutron-rich isotopes. Besides, the densities obtained by the Green's function method can be independent on the space sizes as discussed in Ref. [77], which is determined basically by the proper boundary conditions of the bound states, weakly bound sates and the continuum employed when constructing the Green's functions.

To explore the contributions of different partial waves

on the extended density distributions in Fig. 6, taking the neutron-rich (a) ^{64}Ca, (b) ^{86}Ni, (c) ^{120}Zr, and (d) ^{174}Sn as examples, we plot in Fig. 7 the compositions $\rho_{lj}(r)/\rho(r)$ as functions of the radial coordinate r. It can be clearly seen that outside the nuclear surface referring to the right boundary of the shallow regions of the total nuclear density distributions, it's the orbitals located around the Fermi surface that play the main role of the density distributions. For example, in the neutron-rich ^{64}Ca, the partial waves $p_{1/2}$, $f_{5/2}$, $g_{9/2}$, $s_{1/2}$, and $d_{5/2}$ contribute a lot for the total density in the area of 5 fm $< r <$ 15 fm. Those levels are located within $\sim$ 5 MeV around the Fermi surface as shown in Fig. 8, where the neutron canonical single-particle levels as well as the occupation probabilities are presented. When going further in the coordinate space with $r >$ 15 fm, the contributions of the partial waves $s_{1/2}$ and $d_{5/2}$ with small angular momenta increase evidently while others reduce. In the case of ^{86}Ni, the single-particle levels $2d_{5/2}$, $3s_{1/2}$, and $2d_{3/2}$ are located above the neutron shell of $N = 50$ and close to the Fermi surface, playing the main role of the neutron density distribution. Although the positive state $1g_{7/2}$ is also very close to the Fermi surface, it does little contributions for the density in large coordinate space due to the large centrifugal barrier. For the nucleus ^{120}Zr with the neutron number very close to the closure of $N = 82$, the single-particle levels between the closures $N = 50$ and $N = 82$ including $2d_{5/2}$, $1g_{7/2}$, $3s_{1/2}$, $2d_{3/2}$, and $1h_{11/2}$, contribute a lot for the densities in large coordinate space. The insignificant occupation of the positive state $2f_{7/2}$ leads to little contribution to the density. Regarding to the neutron-rich ^{174}Sn with the neutron number exceeding the closure of $N = 82$, the weakly bound single-particle levels $2f_{7/2}$, $2f_{5/2}$, $3p_{3/2}$, and $3p_{1/2}$ with small angular momentum play the key role for the extended density distributions in the large coordinate space. According to those analysis, we can conclude that the single-particle levels around the Fermi surface and particularly the waves with low angular momenta are the main cause for the extended nuclear density.

In Fig. 8, the particle occupation probabilities v^2 on different canonical levels $\varepsilon_{\rm N}^{\rm can}$ are presented and denoted by the length of the lines. Without pairing, the values of the occupation probabilities v^2 should be either one or zero separated by the Fermi surface. With the effect of pairing, the nucleons occupying the levels below the Fermi surface can be scattered to higher levels, which results in the occupations of the weakly bound states above the Fermi surface and even levels in the continuum. In the neutron-rich nuclei ^{64}Ca, ^{86}Ni, ^{120}Zr, and ^{174}Sn, the number of neutrons $N_\lambda = \sum_{\varepsilon_k > \lambda_{\rm n}} (2j+1)v_k^2$ scattered above the Fermi surface $\lambda_{\rm n}$ are 4.33, 2.51, 0.159, and 0.173, respectively. In the case of ^{64}Ca, the weakly bound single-particle $1g_{9/2}$ contribute around 3.7 neutrons.

To explore the effects of pairing, we plot in Fig. 9 the number of neutrons N_λ scattered above the Fermi surface

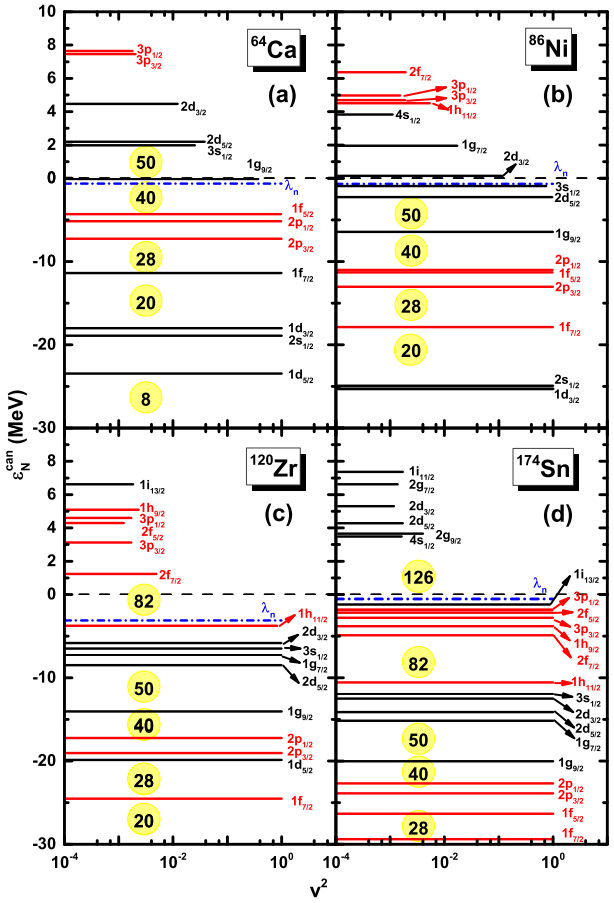

FIG. 8: (Color online) Neutron canonical single-particle levels in the (a) ^{64}Ca, (b) ^{86}Ni, (c) ^{120}Zr, and (d) ^{174}Sn calculated by the Skyrme-HFB theory with the Green's function method. The blue dashed lines represent the Fermi surface. The occupation probabilities v^2 for the canonical orbitals are proportional to the lengths of the lines (in logarithmic scale).

for the (a) Ca, (b) Ni, (c) Zr, and (d) Sn chains obtained by the Skyrme-HFB theory with the Green's function method. It can be seen clearly that substantial neutrons have been scattered from the single-particle levels below the Fermi surface to the weakly bound states above the Fermi surface and even levels in the continuum due to the pairing, especially in the nuclei with the neutron number filling the half-full shells. Besides, very obvious shell structure could be observed. With the number of neutrons reaching a magic number, i.e., $N = 28, 40$ in Ca isotopes, $N = 40, 50$ in Ni isotopes, $N = 50, 82$ in Zr isotopes, and $N = 82, 126$ in Sn isotopes, N_λ is almost zero due to the absence of the pairing for the closed-shell nuclei. Besides, at the points of $N = 32$ in the Ca isotopes, $N = 54, 68$ in the Zr isotopes, and $N = 88$ in the Sn isotopes, very small numbers of neutron N_λ are obtained, which indicate weak pairing in those nuclei. On the other hand, it can also predict the possible existence of sub-shells and new magic numbers. Furthermore, the evolution of N_λ is basically consistent with the trend of

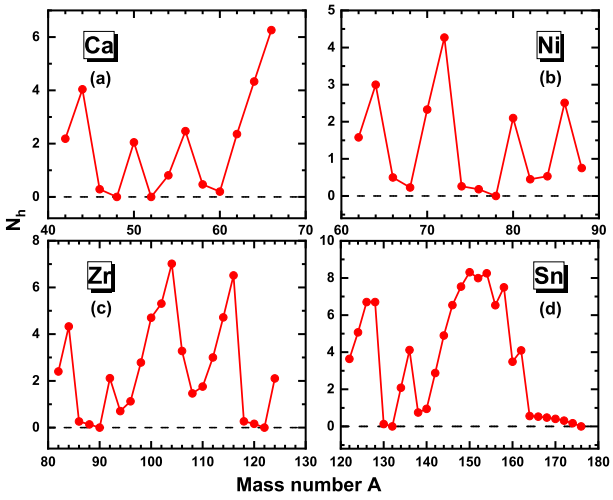

FIG. 9: (Color online) Number of the neutrons N_λ occupying the single-particle levels above the Fermi surface λ_n as a function of the mass number A for the (a) Ca, (b) Ni, (c) Zr, and (d) Sn isotopes calculated by the Skyrme-HFB theory with the Green's function method.

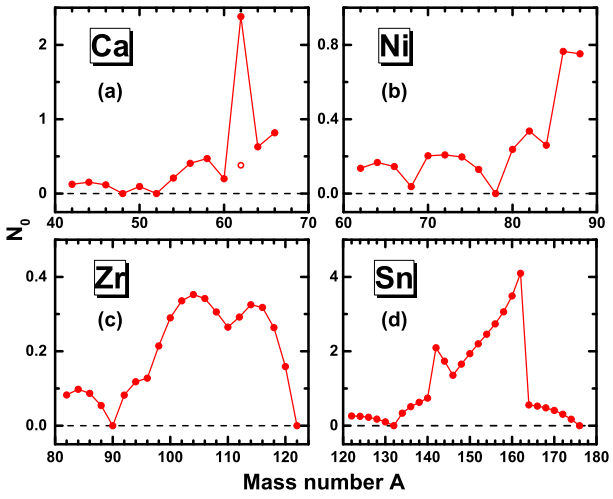

FIG. 10: (Color online) Number of neutrons N_0 occupying in the continuum (above the threshold $\varepsilon = 0$ MeV) as a function of the mass number A for the (a) Ca, (b) Ni, (c) Zr, and (d) Sn isotopes calculated by the Skyrme-HFB theory with the Green's function method.

pair energy $-E_{\rm pair}$ in Fig. 3.

In Fig. 10, we further investigate the number of neutrons occupying the continuum with the single-particle energies $\varepsilon > 0$ MeV, i.e., $N_0 = \sum_{\varepsilon_k>0}(2j+1)v_k^2$. Compared with the number of neutrons N_λ occupying the levels above the Fermi surface, the number of neutrons occupying the continuum N_0 is reduced drastically. For example, in the Ca chain, N_0 is less than one in all isotopes except ^{62}Ca. In ^{62}Ca, the single-particle level $1g_{g/2}$ displays as a low-lying canonical positive state in the continuum with energy of $\varepsilon = 0.198$ MeV and a high occupation probability of $v^2 = 0.197$, resulting in almost 1.979 neutrons occupying it. But in the neighboring ^{60}Ca, very small occupation probability $v^2 = 0.015$ of $1g_{9/2}$ is obtained while in ^{64}Ca, the $1g_{9/2}$ state drops to be a weakly bound level with the energy of $\varepsilon = -0.072$ MeV. After removing the neutron contribution from $1g_{g/2}$ in ^{62}Ca, only 0.38 neutrons are in the continuum, which is denoted by an empty circle in panel (a). Except the Sn chain, the shape of N_0 is very close to those of pairing energy and pairing gap. Although the case of Sn chain becomes very complex, we can still observe the shell structure at $N = 82$ and $N = 126$ where N_0 is almost zero.

V. SUMMARY

In this work, the exotic nuclear properties of neutron-rich Ca, Ni, Zr, and Sn isotopes are examined systematically taking the continuum Skyrme-HFB theory in the coordinate space formulated with the Green's function method, in which the pairing correlations, the couplings to continuum, and the blocking effects for the unpaired nucleon in odd-A nuclei are treated properly.

Firstly, both the two-neutron separation energies S_{2n} and one-neutron separation energies S_n are calculated, which are consistent with the experimental data. Significant differences exist for the drip lines determined by S_{2n} and S_n. In the Ca, Ni, Zr, and Sn isotopes, the drip line nuclei are ^{67}Ca, ^{89}Ni, ^{123}Zr, and ^{177}Sn judging by S_{2n} while ^{60}Ca, ^{86}Ni, ^{122}Zr, and ^{148}Sn according to S_n. Due to the absent contribution of pairing energy by the single unpaired odd neutron, the neutron pairing energies $-E_{\rm pair}$ of the odd-A nuclei are around 2 MeV smaller in comparison with those of the neighboring even-even nuclei. This also explains why the drip lines determined by S_n are much shorter than those by S_{2n}. In addition, from the fluctuation trends of the pairing energy, the traditional neutron magic numbers are clearly displayed, i.e., $N = 28, 40$ in Ca isotopes, $N = 40, 50$ in Ni isotopes, $N = 50, 82$ in Zr isotopes, and $N = 82, 126$ in Sn isotopes.

Secondly, to explore the possible halo structures in the neutron-rich Ca, Ni, Zr, and Sn isotopes, the neutron single-particle structures, the root-mean-square radii, and the density distributions are investigated. In the neutron-rich Ca, Ni, Sn nuclei, especially the weakly bound nuclei close to neutron drip line, the rms radii have sharp increases with significant deviations from the traditional $r \propto A^{1/3}$ rule. Besides, very diffuse spatial density distributions are also observed in those nuclei, which reflects the possible halo phenomenon therein. By analyzing the contribution of different partial waves to the total density, we found that the orbitals located around the Fermi surface and particularly those with low angular momenta are the main cause for the extended nuclear density and large rms radii.

Finally, the number of halo nucleons which could reflects the effects of pairing are discussed. Two different

numbers of neutrons are defined, i.e., N_λ occupying the single-particle levels above the Fermi surface λ_n and N_0 occupying the continuum. We found that the evolutions of N_λ and N_0 with the mass number A are basically consistent with the trend of pairing energy $-E_{\rm pair}$, which supports the key role of the pairing correlations in the halo phenomena.

Acknowledgments

This work was partly supported by the National Natural Science Foundation of China (U2032141), the Natural Science Foundation of Henan Province (202300410479), the Guizhou Provincial Science and Technology Projects (No. ZK[2022]203), the Foundation of Fundamental Research for Young Teachers of Zhengzhou University (JC202041041), and the Physics Research and Development Program of Zhengzhou University (32410217). The theoretical calculation was supported by the nuclear data storage system in Zhengzhou University.

[1] I. Tanihata, Prog. Part. Nucl. Phys. **35**, 505 (1995).
[2] B. Jonson, Phys. Rep. **389**, 1 (2004).
[3] I. Tanihata, H. Savajols, and R. Kanungo, Prog. Part. Nucl. Phys. **68**, 215 (2013).
[4] T. Nakamura, AAPPS Bull. **29**, 19 (2019).
[5] A. C. Mueller and B. M. Sherrill, Annu. Rev. Nucl. Part. Sci. **43**, 529 (1993).
[6] P. Hansen, Nucl. Phys. A **588**, c1 (1995).
[7] R. Casten and B. Sherrill, Prog. Part. Nucl. Phys. **45**, S171 (2000).
[8] A. S. Jensen, K. Riisager, D. V. Fedorov, and E. Garrido, Rev. Mod. Phys. **76**, 215 (2004).
[9] J. Meng, H. Toki, S.-G. Zhou, S.-Q. Zhang, W.-H. Long, and L.-S. Geng, Prog. Part. Nucl. Phys. **57**, 470 (2006).
[10] S. N. Ershov, L. V. Grigorenko, J. S. Vaagen, and M. V. Zhukov, J. Phys. G: Nucl. Phys. **37**, 064026 (2010).
[11] I. Tanihata, H. Hamagaki, O. Hashimoto, Y. Shida, N. Yoshikawa, K. Sugimoto, O. Yamakawa, T. Kobayashi, and N. Takahashi, Phys. Rev. Lett. **55**, 2676 (1985).
[12] T. Minamisono, T. Ohtsubo, I. Minami, S. Fukuda, A. Kitagawa, M. Fukuda, K. Matsuta, Y. Nojiri, S. Takeda, H. Sagawa, and H. Kitagawa, Phys. Rev. Lett. **69**, 2058 (1992).
[13] W. Schwab, H. Geissel, H. Lenske, K. H. Behr, A. Brünle, K. Burkard, H. Irnich, T. Kobayashi, G. Kraus, A. Magel, G. Münzenberg, F. Nickel, K. Riisager, C. Scheidenberger, B. M. Sherrill, T. Suzuki, and B. Voss, Z. Phys. A **350**, 283 (1995).
[14] J. Meng and P. Ring, Phys. Rev. Lett. **77**, 3963 (1996).
[15] J. Meng and P. Ring, Phys. Rev. Lett. **80**, 460 (1998).
[16] S.-G. Zhou, J. Meng, P. Ring, and E.-G. Zhao, Phys. Rev. C **82**, 011301 (2010).
[17] X.-X. Sun and S.-G. Zhou, Sci. Bull. **66**, 2072 (2021).
[18] A. Ozawa, T. Kobayashi, T. Suzuki, K. Yoshida, and I. Tanihata, Phys. Rev. Lett. **84**, 5493 (2000).
[19] T. Otsuka, R. Fujimoto, Y. Utsuno, B. A. Brown, M. Honma, and T. Mizusaki, Phys. Rev. Lett. **87**, 082502 (2001).
[20] M. Rejmund, S. Bhattacharyya, A. Navin, W. Mittig, L. Gaudefroy, M. Gelin, G. Mukherjee, F. Rejmund, P. Roussel-Chomaz, and C. Theisen, Phys. Rev. C **76**, 021304 (2007).
[21] M. Rosenbusch, P. Ascher, D. Atanasov, C. Barbieri, D. Beck, K. Blaum, C. Borgmann, M. Breitenfeldt, R. B. Cakirli, A. Cipollone, S. George, F. Herfurth, M. Kowalska, S. Kreim, D. Lunney, V. Manea, P. Navrátil, D. Neidherr, L. Schweikhard, V. Somà, J. Stanja, F. Wienholtz, R. N. Wolf, and K. Zuber, Phys. Rev. Lett. **114**, 202501 (2015).
[22] S. Chen, J. Lee, P. Doornenbal, A. Obertelli, C. Barbieri, Y. Chazono, P. Navrátil, K. Ogata, T. Otsuka, F. Raimondi, V. Somà, Y. Utsuno, K. Yoshida, H. Baba, F. Browne, D. Calvet, F. Château, N. Chiga, A. Corsi, M. L. Cortés, A. Delbart, J.-M. Gheller, A. Giganon, A. Gillibert, C. Hilaire, T. Isobe, J. Kahlbow, T. Kobayashi, Y. Kubota, V. Lapoux, H. N. Liu, T. Motobayashi, I. Murray, H. Otsu, V. Panin, N. Paul, W. Rodriguez, H. Sakurai, M. Sasano, D. Steppenbeck, L. Stuhl, Y. L. Sun, Y. Togano, T. Uesaka, K. Wimmer, K. Yoneda, N. Achouri, O. Aktas, T. Aumann, L. X. Chung, F. Flavigny, S. Franchoo, I. Gašparić, R.-B. Gerst, J. Gibelin, K. I. Hahn, D. Kim, T. Koiwai, Y. Kondo, P. Koseoglou, C. Lehr, B. D. Linh, T. Lokotko, M. MacCormick, K. Moschner, T. Nakamura, S. Y. Park, D. Rossi, E. Sahin, D. Sohler, P.-A. Söderström, S. Takeuchi, H. Törnqvist, V. Vaquero, V. Wagner, S. Wang, V. Werner, X. Xu, H. Yamada, D. Yan, Z. Yang, M. Yasuda, and L. Zanetti, Phys. Rev. Lett. **123**, 142501 (2019).
[23] X.-X. Sun, J. Zhao, and S.-G. Zhou, Phys. Lett. B **785**, 530 (2018).
[24] A. Zilges, M. Babilon, T. Hartmann, D. Savran, and S. Volz, Prog. Part. Nucl. Phys. **55**, 408 (2005).
[25] P. Adrich, A. Klimkiewicz, M. Fallot, K. Boretzky, T. Aumann, D. Cortina-Gil, U. D. Pramanik, T. W. Elze, H. Emling, H. Geissel, M. Hellström, K. L. Jones, J. V. Kratz, R. Kulessa, Y. Leifels, C. Nociforo, R. Palit, H. Simon, G. Surówka, K. Sümmerer, and W. Waluś, Phys. Rev. Lett. **95**, 132501 (2005).
[26] M. Arnould, S. Goriely, and K. Takahashi, Phys. Rep. **450**, 97 (2007).
[27] J.-W. Xia, W.-L. Zhan, B.-W. Wei, Y.-J. Yuan, M.-T. Song, W.-Z. Zhang, X.-D. Yang, P. Yuan, D.-Q. Gao, H.-W. Zhao, X.-T. Yang, G.-Q. Xiao, K.-T. Man, J.-R. Dang, X.-H. Cai, Y.-F. Wang, J.-Y. Tang, W.-M. Qiao, Y.-N. Rao, Y. He, L.-Z. Mao, and Z.-Z. Zhou, Nucl. Instrum. Meth. A **488**, 11 (2002).
[28] W.-L. Zhan, H.-S. Xu, G.-Q. Xiao, J.-W. Xia, H.-W.

Zhao, and Y.-J. Yuan, Nucl. Phys. A **834**, 694c (2010).
[29] C. Sturm, B. Sharkov, and H. St?cker, Nucl. Phys. A **834**, 682c (2010).
[30] S. Gales, Nucl. Phys. A **834**, 717c (2010).
[31] T. Motobayashi, Nucl. Phys. A **834**, 707c (2010).
[32] M. Thoennessen, Nucl. Phys. A **834**, 688c (2010).
[33] X. H. Zhou, Nucl. Phys. Rev. **35**, 339 (2018).
[34] X. Zhou, M. Wang, Y.-H. Zhang, H.-S. Xu, Y.-J. Yuan, J.-C. Yang, Yu. A. Litvinov, S. A. Litvinov, B. Mei, X.-L. Yan, X. Xu, P. Shuai, Y.-M. Xing, R.-J. Chen, X.-C. Chen, C.-Y. Fu, Q. Zeng, M.-Z. Sun, H.-F. Li, Q. Wang, T. Bao, M. Zhang, M. Si, H.-Y. Deng, M.-Z. Liu, T. Liao, J.-Y. Shi, and Y.-N. Song, Nucl. Sci. Tech. **32**, 37 (2021).
[35] *Relativistic Density Functional for Nuclear Structure*, edited by J. Meng, International Review of Nuclear Physics Vol. 10, (World Scientific, Singapore, 2016).
[36] X.-B. Wei, H.-L. Wei, Y.-T. Wang, J. Pu, K.-X. Cheng, Y.-F. Guo, and C.-W. Ma, Nucl. Sci. Tech. **33**, 155 (2022).
[37] Y.-F. Gao, B.-S. Cai, and C.-X. Yuan, Nucl. Sci. Tech. **34**, 9 (2023).
[38] J. Dobaczewski, W. Nazarewicz, T. R. Werner, J. F. Berger, C. R. Chinn, and J. Dechargé, Phys. Rev. C **53**, 2809 (1996).
[39] J. Meng, Nucl. Phys. A **635**, 3 (1998).
[40] M. Grasso, N. Sandulescu, N. Van Giai, and R. J. Liotta, Phys. Rev. C **64**, 064321 (2001).
[41] N. Sandulescu, L. S. Geng, H. Toki, and G. C. Hillhouse, Phys. Rev. C **68**, 054323 (2003).
[42] L.-G. Cao, and Z.-Y. Ma, Eur. Phys. J. A **22**, 189 (2004).
[43] T. Nakamura, N. Kobayashi, Y. Kondo, Y. Satou, N. Aoi, H. Baba, S. Deguchi, N. Fukuda, J. Gibelin, N. Inabe, M. Ishihara, D. Kameda, Y. Kawada, T. Kubo, K. Kusaka, A. Mengoni, T. Motobayashi, T. Ohnishi, M. Ohtake, N. A. Orr, H. Otsu, T. Otsuka, A. Saito, H. Sakurai, S. Shimoura, T. Sumikama, H. Takeda, E. Takeshita, M. Takechi, S. Takeuchi, K. Tanaka, K. N. Tanaka, N. Tanaka, Y. Togano, Y. Utsuno, K. Yoneda, A. Yoshida, and K. Yoshida, Phys. Rev. Lett. **103**, 262501 (2009).
[44] N. Kobayashi, T. Nakamura, Y. Kondo, J. A. Tostevin, Y. Utsuno, N. Aoi, H. Baba, R. Barthelemy, M. A. Famiano, N. Fukuda, N. Inabe, M. Ishihara, R. Kanungo, S. Kim, T. Kubo, G. S. Lee, H. S. Lee, M. Matsushita, T. Motobayashi, T. Ohnishi, N. A. Orr, H. Otsu, T. Otsuka, T. Sako, H. Sakurai, Y. Satou, T. Sumikama, H. Takeda, S. Takeuchi, R. Tanaka, Y. Togano, and K. Yoneda, Phys. Rev. Lett. **112**, 242501 (2014).
[45] P. Ring and P. Schuck, *The nuclear many-body problem* (Springer Science & Business Media, 2004).
[46] J. Dechargé and D. Gogny, Phys. Rev. C **21**, 1568 (1980).
[47] J. Dobaczewski, H. Flocard, and J. Treiner, Nucl. Phys. A **422**, 103 (1984).
[48] W.-H. Long, P. Ring, N. V. Giai, and J. Meng, Phys. Rev. C **81**, 024308 (2010).
[49] L.-L. Li, J. Meng, P. Ring, E.-G. Zhao, and S.-G. Zhou, Phys. Rev. C **85**, 024312 (2012).
[50] Y. Chen, L.-L. Li, H.-Z. Liang, and J. Meng, Phys. Rev. C **85**, 067301 (2012).
[51] J.-C. Pei, Y.-N. Zhang, and F.-R. Xu, Phys. Rev. C **87**, 051302 (2013).
[52] Y.-N. Zhang, J.-C. Pei, and F.-R. Xu, Phys. Rev. C **88**, 054305 (2013).
[53] J. C. Pei, G. I. Fann, R. J. Harrison, W. Nazarewicz, Y. Shi, and S. Thornton, Phys. Rev. C **90**, 024317 (2014).
[54] Y. Shi, Phys. Rev. C **98**, 014329 (2018).
[55] Y. Gambhir, P. Ring, and A. Thimet, Ann. Phys. **198**, 132 (1990).
[56] S.-G. Zhou, J. Meng, and P. Ring, Phys. Rev. C **68**, 034323 (2003).
[57] M. V. Stoitsov, W. Nazarewicz, and S. Pittel, Phys. Rev. C **58**, 2092 (1998).
[58] M. Stoitsov, J. Dobaczewski, W. Nazarewicz, and P. Ring, Comput. Phys. Commun. **167**, 43 (2005).
[59] K.-Y. Zhang, M.-K. Cheoun, Y.-B. Choi, P. S. Chong, J.-m. Dong, L.-S. Geng, E. Ha, X.-T. He, C. Heo, M. C. Ho, E. J. In, S. Kim, Y. Kim, C.-H. Lee, J. Lee, Z.-P. Li, T.-P. Luo, J. Meng, M.-H. Mun, Z.-M. Niu, C. Pan, P. Papakonstantinou, X.-L. Shang, C.-W. Shen, G.-F. Shen, W. Sun, X.-X. Sun, C. K. Tam, Thaivayongnou, C. Wang, S. H. Wong, X.-W. Xia, Y.-J. Yan, R. W.-Y. Yeung, T. C. Yiu, S.-Q. Zhang, W. Zhang, and S.-G. Zhou, Phys. Rev. C **102**, 024314 (2020).
[60] S. Kim, M.-H. Mun, M.-K. Cheoun, and E. Ha, Phys. Rev. C **105**, 034340 (2022).
[61] E. Tamura, Phys. Rev. B **45**, 3271 (1992).
[62] D. L. Foulis, Phys. Rev. A **70**, 022706 (2004).
[63] E. N. Economou, *Green's Fucntion in Quantum Physics* (Springer-Verlag, Berlin, 2006).
[64] S. T. Belyaev, A. V. Smirnov, S. V. Tolokonnikov, and S. A. Fayans, Sov. J. Nucl. Phys. **45**, 783 (1987).
[65] M. Matsuo, Nucl. Phys. A **696**, 371 (2001).
[66] M. Matsuo, Prog. Theor. Phys. Suppl. **146**, 110 (2002).
[67] M. Matsuo, K. Mizuyama, and Y. Serizawa, Phys. Rev. C **71**, 064326 (2005).
[68] M. Matsuo and Y. Serizawa, Phys. Rev. C **82**, 024318 (2010).
[69] H. Shimoyama and M. Matsuo, Phys. Rev. C **84**, 044317 (2011).
[70] H. Shimoyama and M. Matsuo, Phys. Rev. C **88**, 054308 (2013).
[71] M. Matsuo, Phys. Rev. C **91**, 034604 (2015).
[72] H. Oba and M. Matsuo, Phys. Rev. C **80**, 024301 (2009).
[73] Y. Zhang, M. Matsuo, and J. Meng, Phys. Rev. C **83**, 054301 (2011).
[74] Y. Zhang, M. Matsuo, and J. Meng, Phys. Rev. C **86**, 054318 (2012).
[75] X. Qu and Y. Zhang, Sci. China-Phys. Mech. Astron. **62**, 112012 (2019).
[76] Y. Zhang and X.-Y. Qu, Phys. Rev. C **102**, 054312 (2020).
[77] T.-T. Sun, Z.-X. Liu, L. Qian, B. Wang, and W. Zhang, Phys. Rev. C **99**, 054316 (2019).
[78] J. Meng and S.-G. Zhou, J. Phys. G: Nucl. Phys. **42**, 093101 (2015).
[79] T.-T. Sun, E. Hiyama, H. Sagawa, H.-J. Schulze, and J. Meng, Phys. Rev. C **94**, 064319 (2016).
[80] W.-L. Lu, Z.-X. Liu, S.-H. Ren, W. Zhang, and T.-T. Sun, J. Phys. G: Nucl. Phys. **44**, 125104 (2017).
[81] T.-T. Sun, W.-L. Lu, and S.-S. Zhang, Phys. Rev. C **96**, 044312 (2017).
[82] T.-T. Sun, C.-J. Xia, S.-S. Zhang, and M. S. Smith,

Chin. Phys. C **42**, 025101 (2018).
[83] Z.-X. Liu, C.-J. Xia, W.-L. Lu, Y.-X. Li, J. N. Hu, and T.-T. Sun, Phys. Rev. C **98**, 024316 (2018).
[84] T.-T. Sun, S.-S. Zhang, Q.-L. Zhang, and C.-J. Xia, Phys. Rev. D **99**, 023004 (2019).
[85] C. Chen, Q.-K. Sun, Y.-X. Li, and T.-T. Sun, Sci. China-Phys. Mech. Astron. **64**, 282011 (2021).
[86] Y. Tanimura, H. Sagawa, T.-T. Sun, and E. Hiyama, Phys. Rev. C **105**, 044324 (2022).
[87] T.-T. Sun, S.-Q. Zhang, Y. Zhang, J.-N. Hu, and J. Meng, Phys. Rev. C **90**, 054321 (2014).
[88] T.-T. Sun, W.-L. Lu, L. Qian, and Y.-X. Li, Phys. Rev. C **99**, 034310 (2019).
[89] T.-T. Sun, Z.-M. Niu, and S.-Q. Zhang, J. Phys. G: Nucl. Phys. **43**, 045107 (2016).
[90] S.-H. Ren, T.-T. Sun, and W. Zhang, Phys. Rev. C **95**, 054318 (2017).
[91] C. Chen, Z. P. Li, Y. X. Li, and T.-T. Sun, Chin. Phys. C **44**, 084105 (2020).
[92] Y.-T. Wang and T.-T. Sun, Nucl. Sci. Tech. **32**, 46 (2021).
[93] T.-T. Sun, Sci. Sin.-Phys. Mech. Astron. **46**, 12006 (2016).
[94] T.-T. Sun, L. Qian, C. Chen, P. Ring, and Z.-P. Li, Phys. Rev. C **101**, 014321 (2020).
[95] J. Carbonell, A. Deltuva, A.C. Fonseca, and R. Lazauskas, Prog. Part. Nucl. Phys. **74**, 55 (2014).
[96] M. Shi, J.-G. Guo, Q. Liu, Z.-M. Niu, and T.-H. Heng, Phys. Rev. C **92**, 054313 (2015).
[97] X.-X. Shi, M. Shi, Z.-M. Niu, T.-H. Heng, and J.-Y. Guo, Phys. Rev. C **94**, 024302 (2016).
[98] M. Shi, Z.-M. Niu, and H.-Z. Liang, Phys. Rev. C **97**, 064301 (2018).
[99] M. Wang, W.-J. Huang, F. Kondev, G. Audi, and S. Naimi, Chin. Phys. C **45**, 030003 (2021).
[100] E. Chabanat, P. Bonche, P. Haensel, J. Meyer, and R. Schaeffer, Nucl. Phys. A **635**, 231 (1998).
[101] M. Matsuo, Phys. Rev. C **73**, 044309 (2006).
[102] M. Matsuo, Y. Serizawa, and K. Mizuyama, Nucl. Phys. A **788**, 307 (2007).
[103] X.-W. Xia, Y. Lim, P.-W. Zhao, H.-Z. Liang, X.-Y. Qu, Y. Chen, H. Liu, L.-F. Zhang, S.-Q. Zhang, and J. Meng, At. Data Nucl. Data Tables **121-122**, 1 (2018).
[104] X.-Y. Qu and Y. Zhang, Phys. Rev. C **99**, 014314 (2019).
[105] X. Y. Qu, H. Tong, and S. Q. Zhang, Phys. Rev. C **105**, 014326 (2022).
[106] W. Satuła, J. Dobaczewski, and W. Nazarewicz, Phys. Rev. Lett. **81**, 3599 (1998).
[107] J. Dobaczewski, P. Magierski, W. Nazarewicz, W. Satuła, and Z. Szymański, Phys. Rev. C **63**, 024308 (2001).
[108] Y. A. Litvinov, T. J. Bürvenich, H. Geissel, Y. N. Novikov, Z. Patyk, C. Scheidenberger, F. Attallah, G. Audi, K. Beckert, F. Bosch, M. Falch, B. Franzke, M. Hausmann, T. Kerscher, O. Klepper, H.-J. Kluge, C. Kozhuharov, K. E. G. Löbner, D. G. Madland, J. A. Maruhn, G. Münzenberg, F. Nolden, T. Radon, M. Steck, S. Typel, and H. Wollnik, Phys. Rev. Lett. **95**, 042501 (2005).
[109] K. Hagino and H. Sagawa, Phys. Rev. C **85**, 014303 (2012).
[110] L. J. Wang, B. Y. Sun, J. M. Dong, and W. H. Long, Phys. Rev. C **87**, 054331 (2013).
[111] L. Coraggio, A. Covello, A. Gargano, and N. Itaco, Phys. Rev. C **88**, 041304 (2013).
[112] W. J. Chen, C. A. Bertulani, F. R. Xu, and Y. N. Zhang, Phys. Rev. C **91**, 047303 (2015).
[113] J. Meng and P. Ring, Phys. Rev. Lett. **80**, 460 (1998).
[114] M. Grasso, S. Yoshida, N. Sandulescu, and N. Van Giai, Phys. Rev. C **74**, 064317 (2006).